AGU100 ADVANCING EARTH AND SPACE SCIENCE

Geophysical Research Letters

RESEARCH LETTER
10.1002/2018GL077481

Key Points:
- Artificially generated seismic signals were detected using infrasonic pressure signature
- Barometers exhibit less wind noise on free-flying platforms compared to tethered airborne platforms
- Seismic activity may be detected on airborne platforms on other planets with significant atmospheres

Correspondence to:
S. Krishnamoorthy,
siddharth.krishnamoorthy@jpl.nasa.gov

Citation:
Krishnamoorthy, S., Komjathy, A., Pauken, M. T., Cutts, J. A., Garcia, R. F., Mimoun, D., et al. (2018). Detection of artificially generated seismic signals using balloon-borne infrasound sensors. *Geophysical Research Letters*, *45*, 3393–3403. https://doi.org/10.1002/2018GL077481

Received 6 FEB 2018
Accepted 21 MAR 2018
Accepted article online 26 MAR 2018
Published online 24 APR 2018

©2018. American Geophysical Union. All Rights Reserved.

Detection of Artificially Generated Seismic Signals Using Balloon-Borne Infrasound Sensors

Siddharth Krishnamoorthy[1], Attila Komjathy[1], Michael T. Pauken[1], James A. Cutts[1], Raphael F. Garcia[2], David Mimoun[2], Alexandre Cadu[2], Anthony Sournac[2], Jennifer M. Jackson[3], Voon Hui Lai[3], and Daniel C. Bowman[4]

[1]Jet Propulsion Laboratory, California Institute of Technlogy, Pasadena, CA, USA, [2]Institut Supérieur de l'Aéronautique et de l'Espace-SUPAERO, Toulouse, France, [3]Seismological Laboratory, California Institute of Technology, Pasadena, CA, USA, [4]Sandia National Laboratories, Albuquerque, NM, USA

Abstract We conducted an experiment in Pahrump, Nevada, in June 2017, where artificial seismic signals were created using a seismic hammer, and the possibility of detecting them from their acoustic signature was examined. In this work, we analyze the pressure signals recorded by highly sensitive barometers deployed on the ground and on tethers suspended from balloons. Our signal processing results show that wind noise experienced by a barometer on a free-flying balloon is lower compared to one on a moored balloon. This has never been experimentally demonstrated in the lower troposphere. While seismoacoustic signals were not recorded on the hot air balloon platform owing to operational challenges, we demonstrate the detection of seismoacoustic signals on our moored balloon platform. Our results have important implications for performing seismology in harsh surface environments such as Venus through atmospheric remote sensing.

Plain Language Summary Seismology has traditionally been performed by placing sensors on the ground. However, on Venus, high temperature and pressure on the surface drastically shorten the lifetime of sensors placed on the ground. This is one of the major reasons why we know so little about the interior of Venus. Earthquakes are known to generate pressure waves in the atmosphere at various frequencies. The low-frequency components are found to travel long distances with relatively little damping. Here we demonstrate that these waves can be detected by pressure sensors floating on balloons. By demonstrating that we can detect artificial earthquakes from their atmospheric signature using a pressure sensor suspended on a balloon, we motivate a new way to perform seismology on Venus—by detecting seismic waves while floating at a high altitude, where the temperature and pressure are more benign. The success of this technology offers a compelling alternative to landing on the surface and surviving for long periods of time to study the internal structure of Venus.

1. Introduction

Seismic activity on Earth generates pressure disturbances in the lower atmosphere, of which the low-frequency components travel upward virtually undiminished through the troposphere, stratosphere, and thermosphere, and occasionally couple with the ionosphere. The ionospheric perturbations from large seismic events can be observed from space by measuring perturbations in the total electron content (TEC) with a network of Global Positioning System (GPS) ground stations (e.g., Galvan et al., 2012; Lognonné et al., 2006). While the generation of a significant ionospheric footprint requires a large earthquake, infrasonic pressure signatures (pressure waves with frequencies below 20 Hz) from smaller quakes have been detected from ground-based measurements of pressure variations traveling in the atmosphere (Arrowsmith et al., 2012; Mutschlecner & Whitaker, 2005; Young & Greene, 1982). Infrasound waves generated from a variety of other natural sources such as volcanoes (Johnson & Ripepe, 2011; Matoza et al., 2017), ocean microbarom (Le Pichon et al., 2004), and meteors (Edwards, 2009) have also been observed. Acoustic source theory suggests that acoustic waves from earthquake-induced ground motion are preferentially directed upward (Blackstock, 2000), resulting in a much stronger signal at increasing altitude, which can be observed using balloons or other floating platforms. One example of airborne detection of infrasound is the work of Banister and Hereford (1991), who detected high-altitude pressure waves from underground and surface explosions

using barometer canisters deployed from parachutes. Balloons offer longer measurement lifetimes than parachutes and larger coverage areas with relatively more direct propagation paths than ground-based detectors. Lastly, since balloons float with prevailing winds, they can more effectively minimize wind noise by drastically reducing the wind-relative speed of the acoustic sensor.

Although balloon-based acoustics research has military origins (for instance, the U.S. Air Force's Project Mogul), there has been recent interest in the use of balloon-based infrasound as a tool for scientific investigations. A research team at the University of North Carolina recently conducted two short flights of infrasonic sensors as part of the High-Altitude Student Platform program, resulting in first published balloon-based infrasonic measurements in over 50 years. Results from the High-Altitude Student Platform experiments indicated extremely low levels of wind noise in the Earth's stratosphere compared to the lower troposphere (Bowman & Lees, 2015, 2017). Accessibility to quiet regions in the atmosphere is yet another advantage that balloon platforms possess over a ground-based one for geophysical acoustics research.

Balloon-borne detection of terrestrial infrasound also finds applications in planetary science. A study conducted by the Keck Institute of Space Studies (KISS) in 2014 (Cutts et al., 2015) concluded that balloon-based detection of the upwardly propagating infrasound signatures would be of great advantage in investigating the internal structure of Venus, where surface temperature and pressure are of the order of 460°C and 90 atmospheres, respectively (Wood et al., 1968). These conditions have thus far prevented long-duration seismology experiments on the surface of Venus and are the leading cause for why so little is known about the planet. However, owing to its high density, the atmosphere of Venus can more efficiently couple ground motion due to seismic activity into atmospheric pressure fluctuations and duct the infrasonic component into its upper atmosphere (Garcia et al., 2005), which a balloon floating in relatively benign conditions could detect, thereby enabling long-duration seismology on Venus through remote sensing techniques.

Encouraged by the findings of the KISS study in 2014 and results from recent balloon experiments, JPL along with its partners, Institut Supérieur de l'Aéronautique et de l'Espace (ISAE-SUPAERO) and the Division of Geological and Planetary Sciences at the California Institute of Technology (Caltech), initiated a program to determine the feasibility of measuring seismic infrasound from a floating balloon. As part of this program, our team is investigating ideal flight altitudes and detection thresholds on Venus using the Earth as an analog test bed. Our preliminary calculations show that quakes with moment magnitudes as low as $M_w = 2.0$ may be detected by a balloon floating at 60-km altitude, if pressure variations on the order of 10^{-3} Pa can be detected by the barometer. Barometers used in this work have the capability to measure such weak variations in pressure; however, extraneous noise sources such as wind, balloon movement, and electronic interference pose a challenge to making these measurements. Therefore, we seek to perform a series of incremental flights starting in the lower troposphere and ending in the Earth's stratosphere to determine noise levels, develop noise mitigation strategies, and determine the detection limit of quakes on Venus. As a first step, we conducted an experimental campaign in Nevada in June 2017 to demonstrate the detection of seismic infrasound signals in the Earth's lower atmosphere. The current work discusses results from this experimental campaign and is organized as follows—section 2 describes the experimental setup in Pahrump, NV, and section 3 describes methods used for the analysis of high-precision barometer data and results from these analyses. We draw conclusions from our current results and discuss our future direction in section 4.

2. Experiment at Pahrump, NV

The aim of the seismic infrasound experiment was to produce seismic infrasound signals from a repeatable source and to determine whether acoustic signatures from these artificial earthquakes could be detected by balloon-borne barometers. Further, we sought to establish the noise reduction capability of a floating platform compared to a stationary one. The seismic source utilized for this experiment was a seismic hammer, which weighed 13 metric tons and was dropped from a height of 1.5 m to create weak but repeatable earthquakes (Hampshire & O'Donnell, 2013; Jones et al., 2015). The seismic hammer releases 0.19 MJ of energy (Hampshire & O'Donnell, 2013), compared to approximately 78 GJ released by an earthquake of moment magnitude $M_w = 3.0$. The main advantage of using the hammer is that the entire energy release occurs on the surface, and the quakes generated are extremely repeatable. Pahrump was chosen as the test site primarily for operational reasons—it is far away from sources of urban noise but convenient to transport the hammer from its location in Las Vegas, NV. The test was conducted on 27 June 2017.

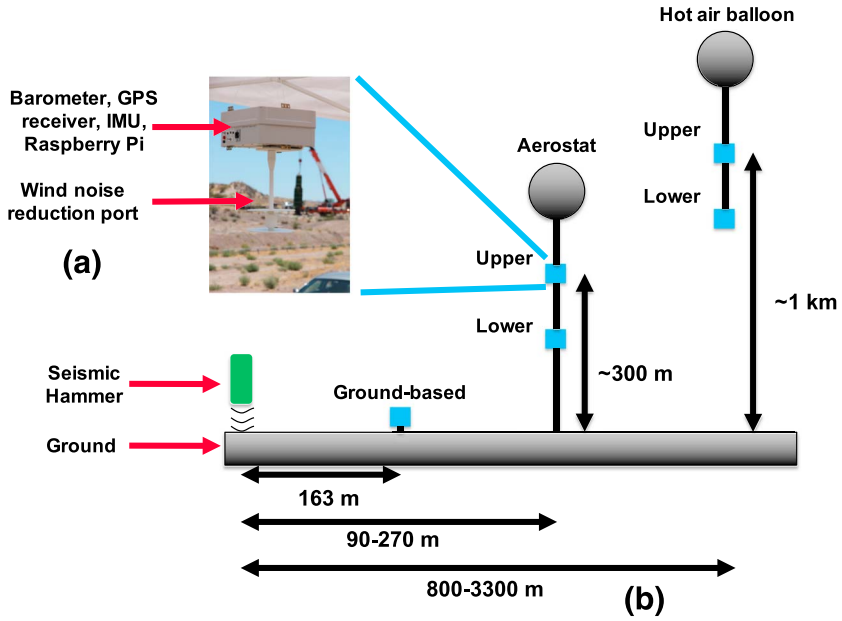

Figure 1. Barometer configuration utilized in the Pahrump experiment. (a) Description of each barometer package containing a barometer, Global Positioning System (GPS) receiver, inertial measurement unit (IMU), a noise reduction port, and a Raspberry Pi computer (b) Deployment plan for the barometers—barometers were deployed in the lower troposphere as the first step toward deploying them on high-altitude balloons in the future.

A large network of geophones was deployed on the ground to measure ground motion caused by the hammering. In addition to the geophones, microphones and Trillium broadband seismometers were also deployed on the ground. Paroscientific Digiquartz 6000-16B-IS barometers with absolute pressure measurement capability between 0.5 and 1.1 bar and parts per million sensitivity were utilized to measure the infrasound signal. Barometers with similar properties but with dynamic range extending down to 0 bar will be utilized in future high-altitude flights, which will be closer analogs to flights on Venus. One barometer was deployed on the ground (ground-based barometer), and two barometers were deployed from a moored balloon (aerostat) on a tether, such that the higher barometer was approximately 300 m above the ground, with the lower barometer suspended 50 m below it. The aerostat was anchored at two locations, approximately 100–120 m away from the hammer. The length of the tether anchoring the aerostat was increased incrementally in order to maximize the delay between surface wave and epicentral infrasound arrivals, until the high winds rendered it unsafe to extend the tether any further. Finally, two barometers were suspended from a similar tether underneath a piloted hot air balloon flying near the hammer site, with the upper barometer reaching a maximum altitude of about 1,000 m above ground level. The hot air balloon was intended as a low-altitude proxy for a drifting long-duration planetary balloon. An illustration of each barometer package and the layout of barometers is shown in Figure 1. The timing of all shots and measurements was coordinated using GPS clocks. The hammer struck the ground 108 times over a period of over 4 hr between 6:53 a.m. and 11:30 a.m. local time. While the ground-based barometer recorded pressure signals from all 108 shots, the hot air balloon barometers were active for shots 1–69, and the aerostat barometers recorded signals from shots 70–108.

3. Barometer Data Analysis

Barometer analysis independent of ground motion is essential to develop a framework for detection and classification of seismic infrasound when ground motion data are not available. The methods discussed below rely only on the location and timing of the seismic disturbance and not on how the seismic disturbance was propagating along the ground. Analysis and fusion of ground motion and barometer data with assistance from our simulation tools is ongoing and will be the subject of future work.

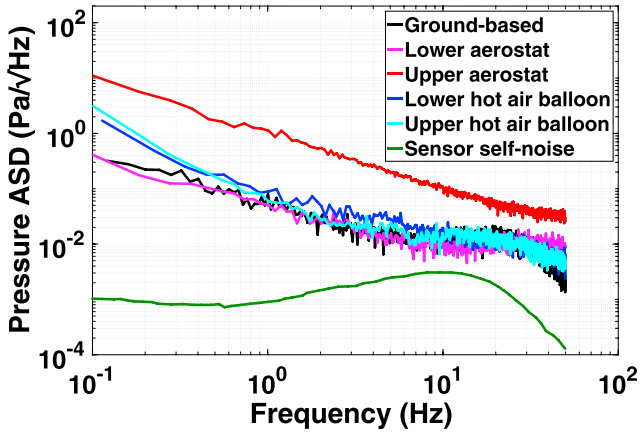

Figure 2. Pressure amplitude spectral density (ASD) from the five barometers. The hot air balloon barometers experience noise levels similar to the ground barometer despite encountering high mean winds at an altitude of 600–1,000 m above ground level.

3.1. Wind Noise

Infrasound signals from seismic events travel long distances but are typically weak. Therefore, wind noise mitigation is important to discriminate the weak signal and avoid false positives. In fact, elaborate wind noise mitigation systems are frequently employed by the Comprehensive Test Ban Treaty Organization at their terrestrial infrasound monitoring stations (Walker & Hedlin, 2009). Since balloons have very large drag compared to their inertia, they travel rapidly in the direction of the prevailing wind, thereby reducing the wind-relative velocity of the barometer. It has previously been argued (Bowman & Lees, 2015, 2017) that the wind noise encountered on a floating barometer in the stratosphere is less than the noise encountered by barometers on the ground. To the best of our knowledge, there has been no analogous comparison made for lower troposphere, where wind noise can often be a major problem. This effect may be demonstrated in our experiment by analyzing the Fourier spectrum of the pressure signal when the balloons were in flight but no shots were taking place, that is, the "quiet" periods. We chose 10 of the cleanest samples (without sporadic or anomalous events from gunshots in the background or wind gusts) during this period of flight, each 12 s long. The number and duration of these samples were chosen to balance the frequency resolution with adequate averaging of the Fourier spectrum. The samples for the hot air balloon were linearly detrended prior to the Fourier transform operation to account for the change in altitude. Figure 2 compares the averaged pressure amplitude spectral densities for the "quiet" samples for all five barometers. It is seen that the barometers on the hot air balloons produce a noise level that is on par with the noise level on the ground-based and lower aerostat barometer, and much lower than the upper aerostat barometer. It is suspected that the noise level in the upper aerostat barometer was further elevated due to interactions with the turbulent wake of the pilot balloon above it, despite being 20 m away.

Since the shots took place in the desert during daytime in the summer, it is reasonable to expect that the atmospheric boundary layer extended at least up to 1 km altitude (Garrat, 1994) above ground level. Therefore, the mean wind encountered at the altitude of the hot air balloon is expected to be substantially larger than the ground-based barometer or the aerostat. However, the hot air balloon mitigates the higher wind by floating with it, thereby producing noise levels that are comparable or lower than the aerostat barometers, which are at a lower altitude. However, by floating with the wind the hot air balloon also drifted far (up to 3.3 km) away from the seismic hammer, leading to much weaker infrasound signal strength. The use of a floating platform increases signal-to-noise ratio (SNR) but impedes the ability to control sampling locations.

3.2. Signal Stacking

With a repeatable seismic source, the infrasound traces for each shot were expected to be similar as well. Therefore, with the knowledge of the positions of the hammer shots and the barometers, the arriving pressure signals could be aligned and stacked using the expected arrival time τ as a reference, whereby

$$\tau = \frac{d}{c_s} \tag{1}$$

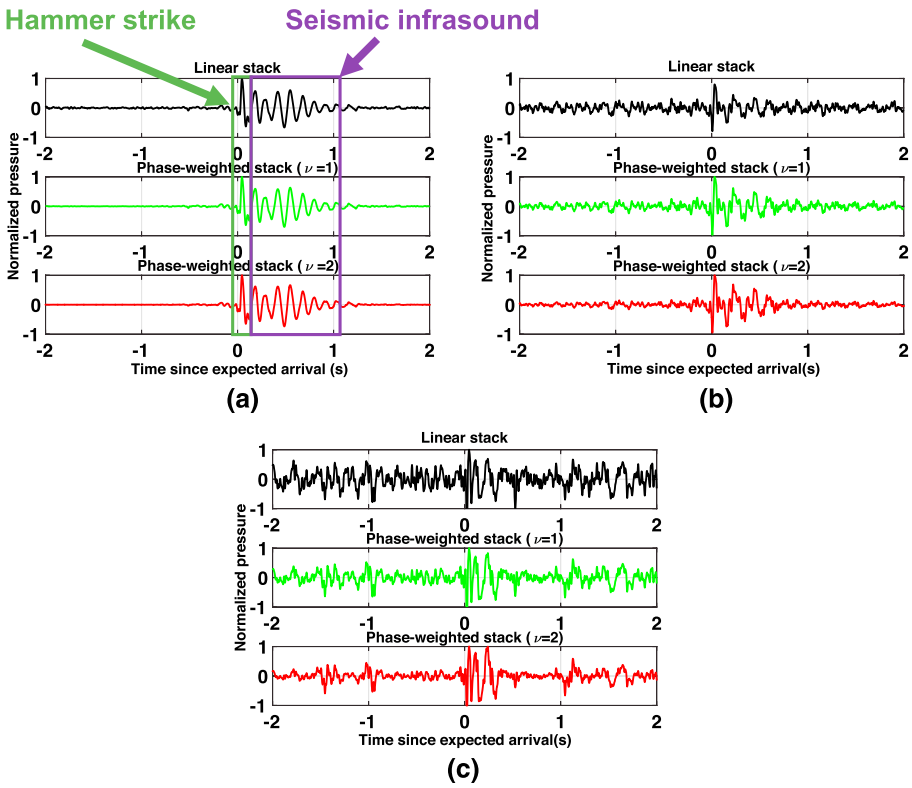

Figure 3. Results from linear and phase-weighted stacking (a) 108 shots for the ground-based barometer, (b) 31 shots each for the lower aerostat barometer, and (c) 31 shots for the upper aerostat barometer. The high-frequency spike of the hammer striking the ground arrives first, followed by oscillations associated with ground motion. Signals are clearest for the ground-based barometer, but the aerostat barometers benefit greatly from using phase-weighted stacking.

where d is the distance between the hammer and the barometer and c_s is the speed of sound, calculated from the temperature supplied by the barometer. The value of τ thus calculated is the expected arrival time for acoustic signals from the epicenter (0 on the time axis in Figure 3). The value of τ ranges from 0.41–0.83 s for the lower aerostat barometer to 0.52–0.92 s for the upper aerostat barometer. Signals from all 108 shots were stacked for the ground-based barometer, whereas signals from 31 shots were used for the aerostat barometers–8 traces each were discarded from the aerostat barometers due to gaps in the pressure-time trace created by the data acquisition algorithm. Unfortunately, pressure signals from the hot air balloon barometers were found to be greatly contaminated with noise from the balloon burner. While it was initially expected that the burner duty cycle would be low and shots would take place when the burner was off, unexpectedly high air temperatures led to a high burner duty cycle and operational complexity prevented synchronization with shots. Additionally, since the hot air balloons drifted far away from the hammer site, the infrasound signal strength was greatly reduced. Further, GPS data recorded at a low rate resulted in large localization errors for the hot air balloon, which led to large uncertainties in the arrival time. For these reasons, the pressure signals measured from the hot air balloon were excluded from further analysis for this work and will be the subject of future studies. Pressure traces from the shots may be stacked by simply averaging individual instances after alignment using the expected arrival time. This strategy works well for the ground-based barometer but does not produce a high SNR for the aerostat barometers. Therefore, we also employed phase-weighted stacking (PWS, described in the appendices; Schimmel & Paulssen, 1997) to enhance coherent periods in the signal and diminish incoherent noise. The results from stacking for the ground-based barometer and the aerostat barometers are shown in Figure 3. The tunable parameter ν referred to in Figure 3 controls how preferentially the coherent periods in the signal are weighted compared to the incoherent periods for PWS (see Appendix A).

The individual instances used for this plot were high-pass filtered at 4 Hz to remove wind noise but retain the pressure spike associated with the hammer striking the ground. The hammer strike clearly appears at exactly the expected arrival time, followed by infrasonic waves associated with the motion of the ground after

the hammer strike. Since PWS is a nonlinear stacking method, the stacked signal is not a pressure signal. Therefore, the values shown in these plots were normalized to their maximum value. The maximum peak-to-peak amplitudes of the linearly stacked signals correspond to 1.03 Pa for the ground-based barometer, 0.34 Pa for the lower aerostat, and 0.24 Pa for the upper aerostat barometer. The signals are clearest for the ground-based barometer but are also clearly discernible in the stacked aerostat records. The advantage of using PWS to enhance signal coherences is most clearly visible for the upper aerostat, which sees a great improvement in its SNR as the value of ν is increased from 0 to 2. From the stacked traces, we can conclude that the aerostat and ground-based barometers clearly detect infrasonic waves from ground motions produced by the hammer strike.

3.3. Time-Frequency Analysis

While signal stacking clearly demonstrates the detection of infrasonic waves by the ground and aerostat barometers, it grants us no insight into detection statistics. We sought to examine individual signals and construct a mathematically consistent framework using which we could determine whether every shot was detected by the barometers. While the relatively clean ground-based barometer signals are easy to analyze in the time domain to determine detection statistics, the same cannot be said for the aerostat barometers with high levels of wind noise. For this reason, we employed the Empirical Wavelet Transform (EWT) technique (Gilles, 2013) to analyze individual shot traces in the time-frequency domain. The EWT technique identifies important modes in a given signal by considering local maxima in its frequency spectrum. Wavelet and scaling functions are then constructed based on this segmentation to produce a spectrogram for the given signal. Doing so allows one to identify any weak modes associated with seismic infrasound that are activated at the expected arrival time of the infrasonic waves. The EWT process was modified for this work to best identify modes associated with seismic infrasound. The modified EWT method for computing the spectrograms is described in the appendices. EWT was recently applied to seismograms by Liu et al. (2016) and is particularly attractive for our usage since it produces relatively sparse spectrograms with few assumptions about the signal being analyzed.

We constructed the "ground truth" for each barometer from its own pressure traces. To accomplish this, we manually scanned the filtered (4–10 Hz band pass) pressure-time traces for each of the ground and aerostat barometers to identify the shots with the clearest seismic infrasound arrivals. The frequency spectra of these traces were averaged and used to determine the segmentation for the EWT process. The resulting spectrograms from this segmentation were then averaged and normalized to produce the "truth spectrogram." Utilizing only signals with the cleanest arrivals in the time domain to construct the truth spectrogram ensures that the artificially constructed ground truth contains all the modes required to identify the arrival of the seismic infrasound signal. It is worth emphasizing that the truth spectrogram for each barometer was constructed using only its own cleanest pressure traces. Since the ground-based barometer had very clear arrivals for all shots, all 108 instances were included in the construction of the ground truth, whereas only 8 each of the 39 shot records available for the aerostat barometers were used. Figure 4 shows the truth spectrogram for the three barometers analyzed. On the left are the raw truth spectrograms, which show all the modes active during the period of measurement. However, we are only interested in modes that show heightened activity near the expected arrival time for the infrasound signal. The right panels in Figure 4 show only the modes that demonstrate heightened activity at the expected arrival time.

Once the ground truth is synthetically constructed from the cleanest barometer traces, other spectrograms can be contrasted from the truth spectrogram using the L-2 norm of the difference to yield the dissimilarity score Δ_j for spectrogram S_j, given by

$$\Delta_j = \mathcal{L}_2(S_j - S_{\text{truth}}) \tag{2}$$

where both spectrograms are masked to include only the frequency bands shown on the right in Figure 4 and a time window of 8 s centered at $t = 0$, the expected arrival time of the seismic infrasound signal. This ensures that dissimilarity from the truth spectrogram is caused primarily by the absence of seismic infrasound modes. We computed dissimilarity scores for each individual shot trace for the three barometers. To provide points of comparison, we also computed the dissimilarity scores for 80 samples (each 8 s long) randomly chosen from times when the balloons were in flight, but the ground was not being struck by the seismic hammer. The results of this analysis are shown in Figure 5—the red line in each figure represents the mean

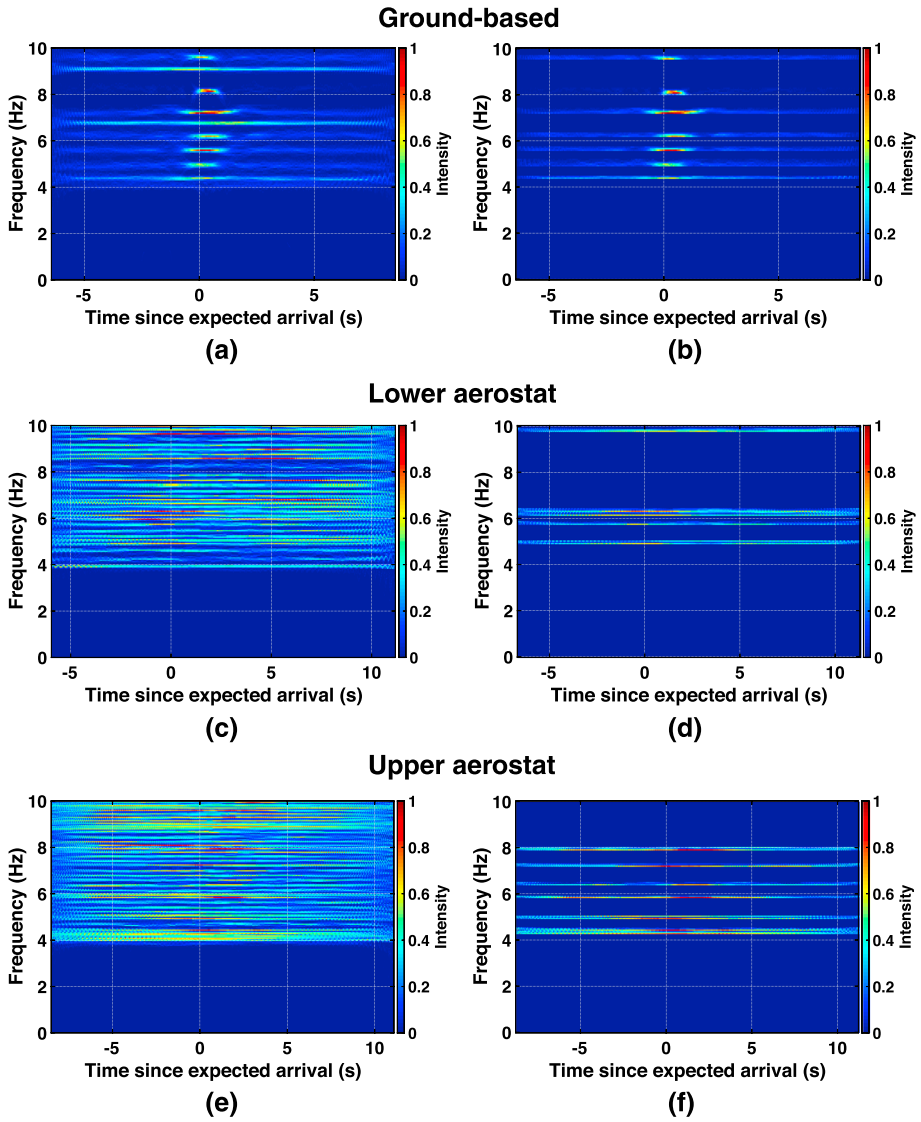

Figure 4. Truth spectrograms for the ground and aerostat barometers. Raw truth spectrograms are depicted on the left panels, only modes that are activated at the expected arrival time are shown in the right panels—all other modes are masked. The intensity shown here is normalized to the maximum value between 4 and 10 Hz—the variation of the intensity serves as a guide for the algorithm to identify seismic infrasound modes: (a and b) Ground-based barometer, (c and d) lower aerostat, (e and f) upper aerostat.

dissimilarity score for the 80 "quiet" period samples, with the dotted line representing the 95% confidence interval computed as

$$\Delta_{q,0.95} = \bar{\Delta}_q - 1.96\frac{\sigma(\Delta_q)}{\sqrt{80}} \tag{3}$$

where $\bar{\Delta}_q$ is the mean of the quiet sample dissimilarity score and σ is the computed standard deviation.

We observe in Figure 5 that dissimilarity scores for most of the shot spectrograms is lower than the mean quiet score. Therefore, at the 95 % confidence level, we can conclude that the shot spectrograms are more similar to the truth spectrograms than the quiet spectrograms. Considering the fact that the truth spectrogram was computed from the traces displaying the cleanest seismic infrasound arrivals and that the dissimilarity scores were computed on the basis of frequency bands and time windows associated with the same, we can conclude that all shots with Δ_j below the mean quiet score detect seismic infrasound arrival.

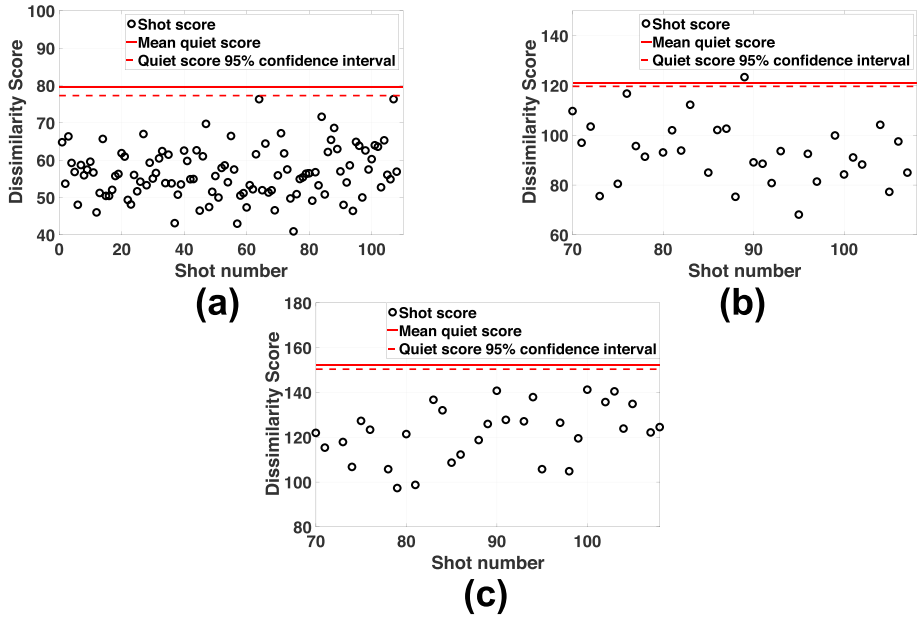

Figure 5. Dissimilarity scores computed for each shot and compared with dissimilarity scores for quiet period samples. (a) Ground-based barometer, (b) lower aerostat, and (c) upper aerostat. Almost all shots display dissimilarity scores below the quiet threshold, meaning that the shot spectrograms are more similar to the truth spectrogram than the quiet spectrograms.

4. Conclusions and Future Work

The experiment at Pahrump, aimed at detecting seismic infrasound from a balloon platform, was the first of its kind. We demonstrated two major results:

1. Wind noise for a barometer on a free-flying balloon platform is comparable to wind noise on a stationary platform on the ground and lower compared to a tethered balloon platform. This is primarily because the flying balloon drifts in the prevailing wind and minimizes the wind-relative velocity of the barometer.
2. It is possible to detect infrasound generated by seismic activity from a balloon. Stacking in the time domain and dissimilarity analysis in the time-frequency domain clearly demonstrate the detection of seismic infrasound by our sensitive barometers. As mentioned before, the hot air balloon was unable to detect the infrasound signal due to operational difficulties. However, with reduced wind noise, it is reasonable to assume that a floating balloon at the location of the aerostat would also have detected the signal. Challenges experienced with using the hot air balloon have been incorporated into the design of future experiments.

Both of the above results have exciting implications for the future of infrasound science from balloons. Since balloons offer larger collection zones, higher SNR, and less directional sensitivity than ground stations, they are naturally suited to performing infrasound science. Several lessons were learned from the challenges encountered in deploying the hot air balloon barometers, which will be used to improve the design of future free-flying balloon experiments.

This technique is also expected to be highly relevant for the remote exploration of planetary interiors in the future, in particular Venus, where the challenge of landing and surviving for long periods of time has thus far rendered seismology impossible. While results presented here are extremely encouraging, further efforts are needed in demonstrating the capability of this technology on Venus. Therefore, in the future, we intend to perform several balloon flights with steadily increasing flight altitudes. Flights are planned over areas of naturally high seismicity to establish the feasibility of recording seismic infrasound on a balloon floating high

in the atmosphere. Finally, we plan to develop sensor systems and detection algorithms that are independent of ground truth knowledge. The success of these endeavors will enable great advances in the study of Venus' interior.

Appendix A: Phase-Weighted Stacking

Phase-weighted stacking is a process by which individual instances of a repeatable signal of interest with noise are combined in a way that coherences are enhanced and incoherent noise in the signal is diminished (Schimmel & Paulssen, 1997). First, the analytical signal $S_i(t)$ for is constructed from each individual instance $s_i(t)$ to yield the instantaneous amplitude $A_i(t)$ and phase $\phi_i(t)$.

$$S_i(t) = s_i(t) + \mathcal{H}\left[s_i(t)\right] = A_i(t)\exp\left[j\phi_i(t)\right] \tag{A1}$$

where $\mathcal{H}[.]$ is the Hilbert transform. A coherence measure $c_i(t)$ is then constructed from the instantaneous phase using

$$c_i(t) = \frac{1}{N}\| \sum_{i=1}^{N} \exp\left[j\phi_i(t)\right] \|. \tag{A2}$$

where N is the number of individual signals being stacked. The coherence measure is close to 1 for parts of the signal that are coherent among the individual instances and close 0 for random noise. The coherence measure may also be windowed and smoothed in time. Finally, the phase-weighted stacked signal $X(t)$ is given by

$$X(t) = \frac{1}{N}\sum_{i=1}^{N} s_i(t)c_i(t)^{\nu} \tag{A3}$$

where the tunable parameter ν controls how preferentially the coherent periods in the signal are weighted compared to the incoherent periods. It may be noted that $\nu = 0$ results in linear stacking. The phase-weighted stacking method is evidently a nonlinear stacking process.

Appendix B: Modified Empirical Wavelet Transform Method for Spectrogram Generation

As mentioned before, the Empirical Wavelet Transform procedure creates sparse spectrograms of time series with few assumptions about the nature of the signal. The procedure followed to generate the spectrograms displayed in this work is as follows (adapted from Gilles, 2013):

1. Consider a given Fourier spectrum $\mathcal{F}(\omega)$. In our case this was the average frequency spectrum of the pressure traces with the cleanest infrasonic arrivals. The spectrum $\mathcal{F}(\omega)$ is segmented into N contiguous segments, such that each segment contains exactly one local maximum and the boundaries of the segment were located at the first local minimum before and after the local maximum contained inside the segment. We ignored peaks that were likely part of a larger structure by ignoring any maxima j with low prominence $P_j < 0.1$, with prominence defined as

$$P_j = \left|\frac{\mathrm{MAX}_j - \mathrm{MIN}_j}{0.5\left(\mathrm{MAX}_j + \mathrm{MIN}_j\right)}\right| \tag{B1}$$

   where MAX_j is the amplitude of peak j and MIN_j is the amplitude of the next local minimum. The number of segments N was increased till the spectrogram showed no changes; that is, all relevant local maxima in the 4- to 10-Hz band were segmented. The values of N for the ground, lower aerostat, and upper aerostat barometers were 15, 37, and 49 respectively.
2. The Fourier axis was normalized to $[0, \pi]$. Let the location of the boundaries of the segments be β_i where $i = 0, 1, 2 \ldots N$, $\beta_0 = 0$, and $\beta_N = \pi$. Then the empirical scaling function $\phi_i(\omega)$ and wavelets $\psi_i(\omega)$ for each mode i are constructed using the following expressions:

$$\phi_i(\omega) = \begin{cases} 1, & \text{if } |\omega| \le (1-\gamma)\beta_i \\ \cos\left[\frac{\pi}{2}\tau\left(\frac{|\omega|-(1-\gamma)\beta_i}{2\gamma\beta_i}\right)\right], & \text{if } (1-\gamma)\beta_i \le |\omega| \le (1+\gamma)\beta_i \\ 0, & \text{otherwise} \end{cases} \tag{B2}$$

$$\psi_i(\omega) = \begin{cases} 1, & \text{if } (1+\gamma)\beta_i \le |\omega| \le (1-\gamma)\beta_{i+1} \\ \cos\left[\frac{\pi}{2}\tau\left(\frac{|\omega|-(1-\gamma)\beta_{i+1}}{2\gamma\beta_{i+1}}\right)\right], & \text{if } (1-\gamma)\beta_{i+1} \le |\omega| \le (1+\gamma)\beta_{i+1} \\ \sin\left[\frac{\pi}{2}\tau\left(\frac{|\omega|-(1-\gamma)\beta_i}{2\gamma\beta_i}\right)\right], & \text{if } (1-\gamma)\beta_i \le |\omega| \le (1+\gamma)\beta_i \\ 0, & \text{otherwise} \end{cases} \tag{B3}$$

where $\tau(x)$ is an arbitrary function such that

$$\tau(x) = \begin{cases} 0, \text{ if } x \le 0 \text{ and } \tau(x) + \tau(1-x) = 1 \forall x \in [0,1] \\ 1, \text{ if } x \ge 1 \end{cases} \tag{B4}$$

and γ is a numerical factor that defines the width of the transition phase between two consecutive segments on the frequency axis.

3. Finally, the detail coefficients for a given pressure trace $p(t)$ are given by

$$W_D(i,t) = \langle p, \psi_n \rangle = \int p(u)\overline{\psi_i(u-t)}\mathrm{d}u, \tag{B5}$$

and the approximation coefficients are given by

$$W_D(0,t) = \langle p, \phi_1 \rangle = \int p(u)\overline{\phi_1(u-t)}\mathrm{d}u. \tag{B6}$$

The approximation and detail coefficients are then utilized to generate spectrograms of the type seen in Figure 4.

Acknowledgments
Contributions from JPL authors were made possible by research carried out with support from an internal research and technology grant at the Jet Propulsion Laboratory, California Institute of Technology, under a contract with the National Aeronautics and Space Administration. Contributions from ISAE authors were funded by ISAE-SUPAERO, la Délégation Générale de l'Armement (DGA), and le site du Centre National d'Études Spatiales (CNES). The authors would like to thank Gerald Walsh, Giorgio Savastano, Sharon Kedar, Kirk Barrow, and others from JPL, NASA Armstrong Flight Research Center, and HH Seismic for their support leading up to and during the Pahrump experiment. We also acknowledge the Front Sight Firearms Training Institute for providing us with the test site for this experiment. Sandia National Laboratories is a multimission laboratory managed and operated by National Technology & Engineering Solutions of Sandia, LLC, a wholly owned subsidiary of Honeywell International Inc., for the U.S. Department of Energy's National Nuclear Security Administration under contract DE-NA0003525. The views expressed in the article do not necessarily represent the views of the U.S. Department of Energy or the United States Government. Data used to generate results presented here have been uploaded to a publicly accesible FigShare repository with doi:10.6084/m9.figshare.6137507.

References

Arrowsmith, S. J., Burlacu, R., Pankow, K., Stump, B., Stead, R., Whitaker, R., & Hayward, C. (2012). A seismoacoustic study of the 2011 January 3 Circleville earthquake. *Geophysical Journal International*, *189*(2), 1148–1158. https://doi.org/10.1111/j.1365-246X.2012.05420.x

Banister, J. R., & Hereford, W. V. (1991). Observed high-altitude pressure waves from an underground and a surface explosion. *Journal of Geophysical Research*, *96*(D3), 5185–5193. https://doi.org/10.1029/90JD02640

Blackstock, D. (2000). *Fundamentals of physical acoustics*. A Wiley-Interscience publication, Wiley.

Bowman, D. C., & Lees, J. M. (2015). Infrasound in the middle stratosphere measured with a free-flying acoustic array. *Geophysical Research Letters*, *42*, 10,010–10,017. https://doi.org/10.1002/2015GL066570

Bowman, D. C., & Lees, J. M. (2017). A comparison of the ocean microbarom recorded on the ground and in the stratosphere. *Journal of Geophysical Research: Atmospheres*, *122*, 9773–9782. https://doi.org/10.1002/2017JD026474

Cutts, J. A., Stevenson, D. J., Mimoun, D., et al. (2015). Probing the interior structure of Venus (Tech. Rep.). Pasadena, CA: Keck Institute for Space Studies.

Edwards, W. N. (2009). Meteor generated infrasound: Theory and observation. In A. Le Pichon, E. Blanc, & A. Hauchecorne (Eds.), *Infrasound monitoring for atmospheric studies* (pp. 361–414). Dordrecht, Netherlands: Springer. https://doi.org/10.1007/978-1-4020-9508-5_12

Galvan, D. A., Komjathy, A., Hickey, M. P., Stephens, P., Snively, J., Song, Y. T., et al. (2012). Ionospheric signatures of Tohoku-oki tsunami of March 11, 2011: Model comparisons near the epicenter. *Radio Science*, *47*, RS4003. https://doi.org/10.1029/2012RS005023

Garcia, R., Lognonné, P., & Bonnin, X. (2005). Detecting atmospheric perturbations produced by Venus quakes. *Geophysical Research Letters*, *32*, L16205. https://doi.org/10.1029/2005GL023558

Garrat, J. R. (1994). Review: The atmospheric boundary layer. *Earth-Science Reviews*, *37*(1), 89–134. https://doi.org/10.1111/j.1365-246X.2012.05420.x

Gilles, J. (2013). Empirical wavelet transform. *IEEE Transactions on Signal Processing*, *61*(16), 3999–4010. https://doi.org/10.1109/TSP.2013.2265222

Hampshire, J. B., & O'Donnell, J. (2013). The seismic hammer. In *Seismic Instrumentation Technology Symposium*. Albuquerque, New Mexico.

Johnson, J. B., & Ripepe, M. (2011). Volcano infrasound: A review. *Journal of Volcanology and Geothermal Research*, *206*(3), 61–69. https://doi.org/10.1016/j.jvolgeores.2011.06.006

Jones, K. R., Abbot, R. E., Hampshire, J. B., White, R., Marcillo, O., & Whitaker, R. W. (2015). Infrasound observations from a seismo-acoustic hammer source at the Nevada National Security Site. *Seismological Research Letters*, *86*(2B), 533–745. https://doi.org/10.1785/0220150017

Le Pichon, A., Maurer, V., Raymond, D., & Hyvernaud, O. (2004). Infrasound from ocean waves observed in Tahiti. *Geophysical Research Letters*, *31*, L19103. https://doi.org/10.1029/2004GL020676

Liu, W., Cao, S., & Chen, Y. (2016). Seismic time-frequency analysis via empirical wavelet transform. *IEEE Geoscience and Remote Sensing Letters*, *13*(1), 28–32. https://doi.org/10.1109/LGRS.2015.2493198

Lognonné, P., Artru, J., Garcia, R., Crespon, F., Ducic, V., Jeansou, E., et al. (2006). Ground-based GPS imaging of ionospheric post-seismic signal. *Planetary and Space Science*, *54*(5), 528–540. https: //doi.org/10.1016/j.pss.2005.10.021

Matoza, R. S., Jolly, A., Fee, D., Johnson, R., Chouet, B., Dawson, P., et al. (2017). Seismo-acoustic wavefield of Strombolian explosions at Yasur volcano, Vanuatu, using a broadband seismo-acoustic network, infrasound arrays, and infrasonic sensors on tethered balloons. *The Journal of the Acoustical Society of America*, *141*(5), 3566–3566. https://doi.org/10.1121/1.4987573

Mutschlecner, J. P., & Whitaker, R. W. (2005). Infrasound from earthquakes. *Journal of Geophysical Research*, *110*, D01108. https://doi.org/10.1029/2004JD005067

Schimmel, M., & Paulssen, H. (1997). Noise reduction and detection of weak, coherent signals through phase-weighted stacks. *Geophysical Journal International*, *130*(2), 497–505. https://doi.org/10.1111/j.1365-246X.1997. tb05664.x

Walker, K. T., & Hedlin, M. A. (2009). A review of wind-noise reduction methodologies. In A. Le Pichon, E. Blanc, & A. Hauchecorne (Eds.), *Infrasound Monitoring for Atmospheric Studies* (pp. 141–182). Dordrecht, Netherlands: Springer. https://doi.org/10.1007/978-1-4020-9508-5_5

Wood, A. T., Wattson, R. B., & Pollack, J. B. (1968). Venus: Estimates of the surface temperature and pressure from radio and radar measurements. *Science*, *162*(3849), 114–116. https://doi.org/10.1126/science.162.3849.114

Young, J. M., & Greene, G. E. (1982). Anomalous infrasound generated by the Alaskan earthquake of 28 March 1964. *The Journal of the Acoustical Society of America*, *71*(2), 334–339. https://doi.org/10.1121/1.387457